

---

# AUTOMATED CLASSIFICATION OF NANOPARTICLES WITH VARIOUS ULTRASTRUCTURES AND SIZES

---

**Claudius Zelenka, Kolja Strohm, Akram Kadoura, Reinhard Koch**  
Department of Computer Science, Kiel University, Christian-Albrechts-Platz 4,  
24118 Kiel, Germany

**Marius Kamp, Lorenz Kienle**  
Institute for Materials Science, Synthesis and Real Structure, Kiel University, Kaiserstr. 2,  
24143 Kiel, Germany  
Kiel Nano, Surface and Interface Science KiNSIS, Kiel University, Christian-Albrechts-Platz 4,  
D-24118 Kiel, Germany  
corresponding author Lorenz Kienle lk@tf.uni-kiel.de

**Jacob Johny**  
Technical Chemistry I and Center for Nanointegration Duisburg-Essen (CENIDE),  
University of Duisburg-Essen, Universitatstr. 7, 45141 Essen, Germany

July 29, 2022

## ABSTRACT

Accurately measuring the size, morphology, and structure of nanoparticles is very important, because they are strongly dependent on their properties for many applications. In this paper, we present a deep-learning based method for nanoparticle measurement and classification trained from a small data set of scanning transmission electron microscopy images. Our approach is comprised of two stages: localization, i.e., detection of nanoparticles, and classification, i.e., categorization of their ultrastructure. For each stage, we optimize the segmentation and classification by analysis of the different state-of-the-art neural networks. We show how the generation of synthetic images, either using image processing or using various image generation neural networks, can be used to improve the results in both stages. Finally, the application of the algorithm to bimetallic nanoparticles demonstrates the automated data collection of size distributions including classification of complex ultrastructures. The developed method can be easily transferred to other material systems and nanoparticle structures.

## 1 Introduction

Commercial computer programs are widely used to analyze the number and size distribution of homogeneous particle samples. But the examination of nanoparticles (NPs) with different ultrastructures, sizes, overlays, and complex contrast formation in scanning transmission electron microscopy (STEM) images overcharges these programs [1]. Detection of NPs with variable contrast is not reliable, because a uniform threshold is applied to the image. To overcome this obstacle, an approach involving artificial intelligence and deep learning is chosen [2, 3]. Such an algorithm, containing neural networks, can be trained to classify the ultrastructure of NPs. In the training routine, manually annotated images are inserted to optimize the recognition patterns. Kharin [4], demonstrated the detection of NPs in scanning electron microscopy images based on neural networks trained with semi-synthetic data.

With our approach, we aim to work towards tackling challenging imaging settings, which include a variety of NPs that can be seemingly overlapping, or subject of low contrast. These challenging situations occur in a large variety and the training data for the deep-learning approach should reflect that. In practice, however, this is not always the case. For instance, in our training set, not all overlapping situations are represented adequately and we have an imbalance between

examples of solid solution (SoSo) and core shell (CS) ultrastructure (Figure 1 a) i) and a) ii), respectively). Exactly these difficult conditions require the application of advanced neural networks in a multi-step process. In particular, the approach includes synthetic data generation and augmentation to reduce the number of training images and to increase the accuracy or the classification.

Our approach is structured in two parts, that are illustrated in Figure 2. Firstly, the detection, which provides the localization and size of each particle, and secondly the classification, which determines the ultrastructure of the NPs. Particularly challenging is the partition of detected structures into distinct ultrastructures, and training this part separately from the classification allows training even if images show a very uneven distribution of ultrastructures.

Next to the size of the NPs, their morphology and ultrastructure are important parameters that are strongly related to their properties [5, 6, 7]. For instance, Fe-Au CS NPs are used for medical applications [8], while SoSo NPs are applied for electro-catalytic oxygen evolution reactions [9]. The generation of significant size distributions requires the statistical analysis of a large number of NPs (>500), which is very time consuming due to manual annotation procedures.

In particular, laser ablation in liquids generates SoSo and CS NPs with a yield that is strongly dependent on target composition, liquid medium, and ablation parameters [10, 11, 12, 13, 14]. Up to now, this classification is performed by manual annotation, nevertheless, the application of the presented algorithm will allow automatic generation of size distributions and classification of the NPs ultrastructure. We demonstrate the applicability of the developed method in the case studies of Au-Co and Au-Fe NPs generated by pulsed laser ablation in liquid.

## 2 Material and Methods

An 8 ns Nd:YAG laser (RofinSinar Technologies, Plymouth) at 1064 nm with a repetition rate of 15 kHz and a fluence of  $3.85 \text{ J/cm}^2$ , and a 10 ps (Ekspla) Nd:YAG laser at 1064 nm with a repetition rate of 100 kHz and a fluence of  $3.1 \text{ J/cm}^2$  were used to ablate the NPs from Au-Fe alloy targets as well as pressed micropowder targets in case of Au-Co with different compositions in acetone. An F-theta lens with a focal length of 100 mm was used to focus the laser beam onto the respective target surface for both systems. The ablations were performed in a batch chamber containing 40 mL of the solvent in a horizontal laser configuration. During the ablation, the laser beam was scanned in a spiral pattern over the target using a galvanometric scanner and liquid rotation was enabled by a flow chamber for enhanced NP production. More details on the NP synthesis can be found elsewhere [10, 11, 14, 12, 13]. TEM studies of the dispersed samples were performed on copper grids with a Lacey carbon film (Plano GmbH), a Tecnai F30 STWIN  $G^2$ , with 300 kV accelerating voltage, was used. Z-contrast images were acquired with a high-angle annular dark-field (HAADF)-STEM detector. The Z-contrast images allow direct identification of the ultrastructure of NPs. The chemical composition was measured using energy dispersive X-ray (EDX) spectroscopy with a Si/Li detector (EDAX system).

The neural networks for NPs detection are based on [15] and are implemented in PyTorch [16], while the augmentation and classification are implemented in Tensorflow [17].

## 3 Detection

### 3.1 Annotation

The data set consists of HAADF-STEM images of size 1024x1024. Among 78 images, 48 were split into training, 20 for validation and 10 for testing. There are 200-600 NPs depicted in every image. Many NPs overlap, so that the contrast in the image is partially formed by several superimposed particles. To be able to learn a detection model, we need to annotate this situation, which means that in this overlapping situation, both the foreground and background NPs must be annotated in their entire shape. As seen in Figure 1a), the NPs are mostly of a spherical shape. This motivates the annotation approach. We annotate the diameter of the NPs in the training images, assuming a spherical shape, a ground truth image is generated. An example with filled colors for easier viewing is shown in Figure 1b). Note that NPs which are overlapping in the image are annotated correctly. Meaning that these pixels belong to two NPs at once.

### 3.2 Training and Model

In recent years, artificial intelligence has made large improvements in object detection algorithms. In the case of NPs, we are interested not only in detecting them in general but also in distinguishing each particle or instance, i.e., instance segmentation. Mask-RCNN [18] is a widely used approach for instance segmentation. Its working principle is as follows. A Backend neural network is used to transform the image into the feature maps. From these maps, different object proposals are generated and with some intermediate steps for each proposal the relevant part of the network response is aggregated using a so-called ROI-align layer and fed into different network heads (Figure 2).

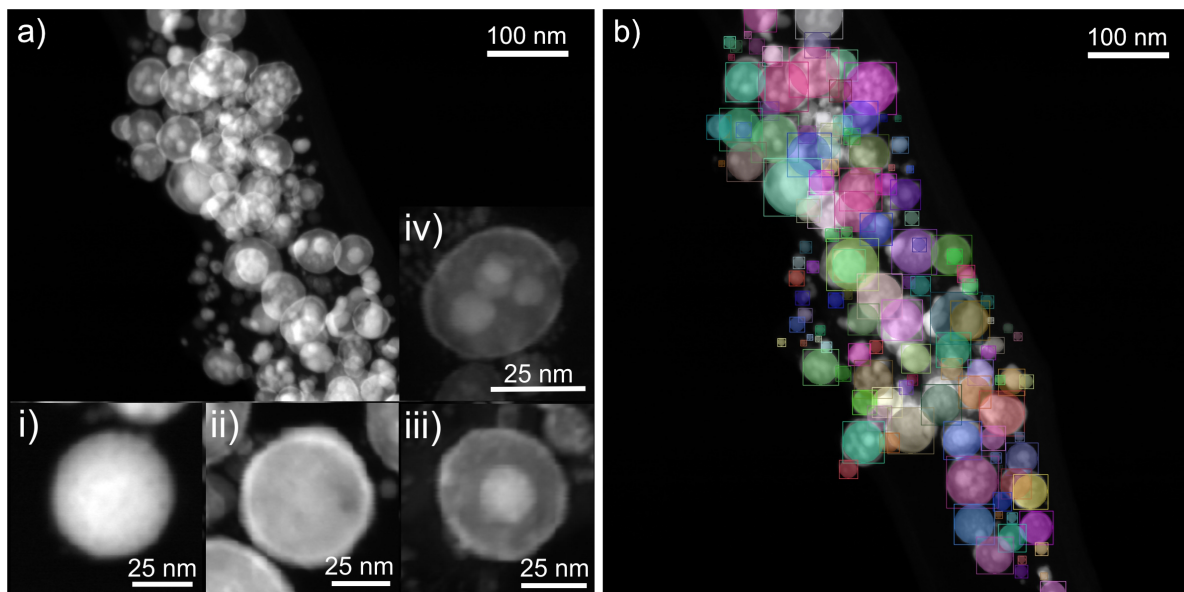


Figure 1: HAADF-STEM image of Au-Fe NPs a) without annotation, the inset shows a SoSo i), a CS ii), a NCS iii), and a NCS with multiple nested cores iv) NP. HAADF-STEM image of Au-Fe NPs b) annotated with filled colors for easier viewing. Different colors mark individual instances.

Most important is the segmentation head which generates a mask of pixels belonging to an object and the classification head, which decides to which object class (particle or background), if any, this bounding box belongs. The bounding box regression head is used to adjust the bounding box to the object. This is how the detection works in principle. The algorithm uses a HAADF-STEM image (see Figure 1 a) as input image and marks the position of NPs by bounding boxes (see Figure 1 b), which are used to extract individual NPs from the images.

Built on Mask-RCNN, Mask Scoring RCNN [19], and Cascade Mask-RCNN [20] further improve the accuracy of the detection. Mask Scoring RCNN [19] is an improvement on Mask-RCNN. During training, the output of the ROI-align layer and the predicted mask are used to predict the intersection over the union between annotation object and mask. This should lead to more accurate detection and better training performance.

The output of the bounding box regression should be a better estimate of the object outline than the region of interest (ROI) proposal used to extract the segment of the ROI-align layer. Therefore, in Cascade Mask-RCNN [20], the output of the bounding box regression is used in another round of ROI-align extraction from the feature maps. This process is repeated ("cascaded") several times.

A flow chart, shown in Figure 2, summarizes the working principle of the algorithm explained above for an image with three NPs. The output of the detection pipeline, illustrated in part 1 (blue), generates a bounding box for every particle, with a classification score signifying the probability of the bounding box containing a particle or background, and finally a mask showing which part of the bounding box belongs to the NP. Further details for the ultrastructure classification presented in part two (green) are discussed in Section 4.

Due to the class imbalance and since our aim is to separately augment and improve the detection and classification, we do not use the classification branch of Mask-RCNN for different kinds of NPs, but we solve this problem with a separate approach as described in Section 4 and illustrated in Figure 2 in part 1.

### 3.3 Generation of additional training data

Not only the manual annotation of NP images is tedious for evaluation, also for training purposes. Therefore, we want to generate additional training data, with realistic annotations to extend the training data and thus to improve the detection performance.

The general idea is to extract NPs from the annotation and randomly place them on a black background. This direct approach is applied in Figure 3 and as can be seen, for a realistic look, more effort is necessary, because the circle-annotations are not accurate enough, especially if we want to consider overlapping NPs in the image.

We use a semantic segmentation U-Net [21] with ResNet50 [22] backbone to generate a probability prediction for each pixel whether it represents a NP or not. Using a threshold, this allows the extraction of particle-groups. For each group,

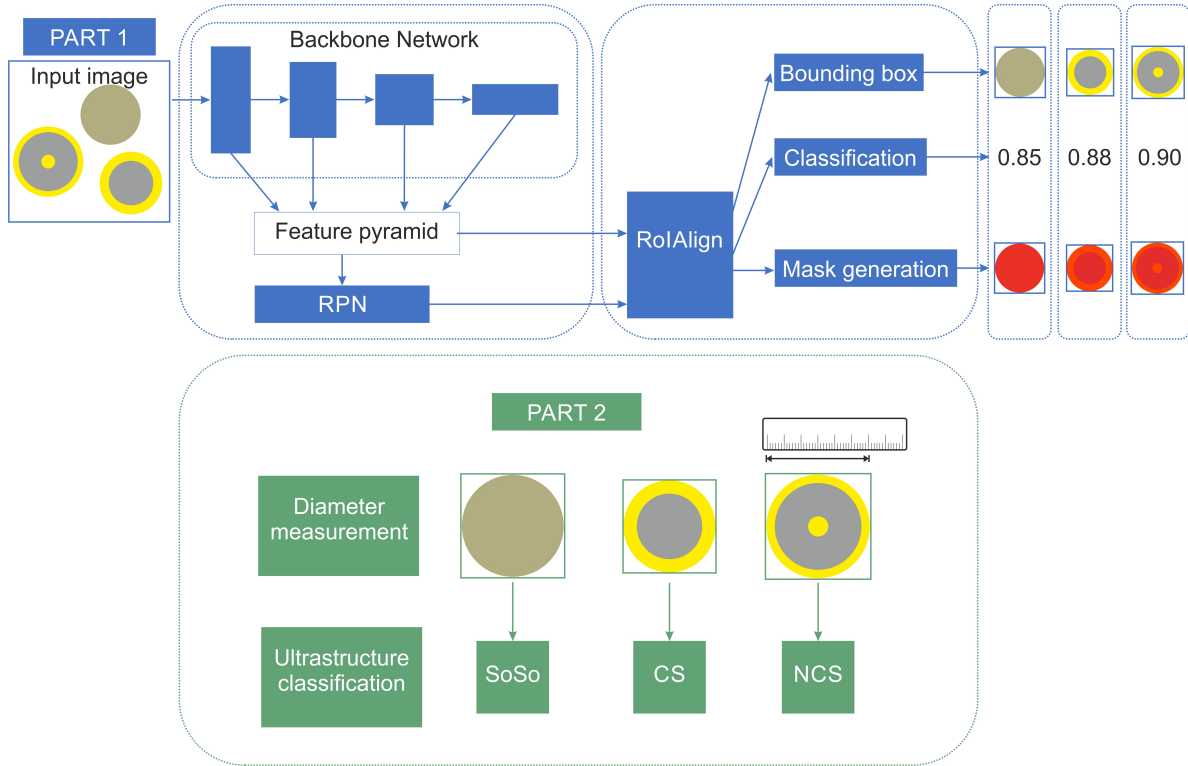


Figure 2: The diagram shows the principle of the two-stage algorithm developed for the detection and categorization of NPs. Part 1 (blue) shows the detection of NPs, Part 2 (green) illustrates how the NPs are assigned to the different ultrastructure classes. The algorithm is demonstrated with an exemplary input image.

we check if circle annotations are available and discard it, if the overlap is not large enough. Some padding is added to each particle for smoother edges and the prediction probability is used as the alpha-transparency channel in the image.

To achieve a greater variety of NPs, the extracted NPs and particle-groups are augmented by rotation and scaling, variation of brightness, and small Gaussian noise. Real images do not show an equal spatial distribution of NPs (see Figure 1 as an example), instead, they appear slightly grouped. To consider this, we also place generated NPs in iteratively generated clusters.

Furthermore, real images exhibit a small halo effect around bright NPs. A physically-based model for this process is difficult because it requires a model of the interaction of the electron beam with the NPs and their environment, therefore, we simulate this effect by smearing the brightness in a randomized direction. A combination of all these steps leads visually to very realistic NPs as shown in Figure 3b. An evaluation of whether these images can be used to train a better detection is conducted in Section 3.4.

### 3.4 Evaluation

To provide an impression of the detection quality a set of qualitative results as images overlaid with detections is shown in Figure 4 a-f). We can see that the detection results are very good even for difficult examples and almost all particles are correctly detected. Slight imperfections can be seen with strongly overlapping NPs and some small NPs with unclear boundaries are missed, but we do not consider this to be an obstacle to the intended application, see Section 5.

To see how the different improvements outlined in previous sections impact the detection performance, an evaluation with the Mean Average Precision (MAP) measure as defined in [23] was performed. Recall describes the percentage of the particles which were detected, precision notes how detections match true particles. While both properties are desirable, there is obviously a trade-off, which we can control by setting a threshold on the classification score in the detection part of the method. A higher threshold leads to a very high recall with few detections, while a lower threshold leads to lower precision with a higher number of detection. MAP is the standard measure for instance segmentation algorithms and roughly consists of the sum under the precision-recall curve for a range of threshold levels. It allows us to take this trade-off into account and to evaluate the detection unbiased.

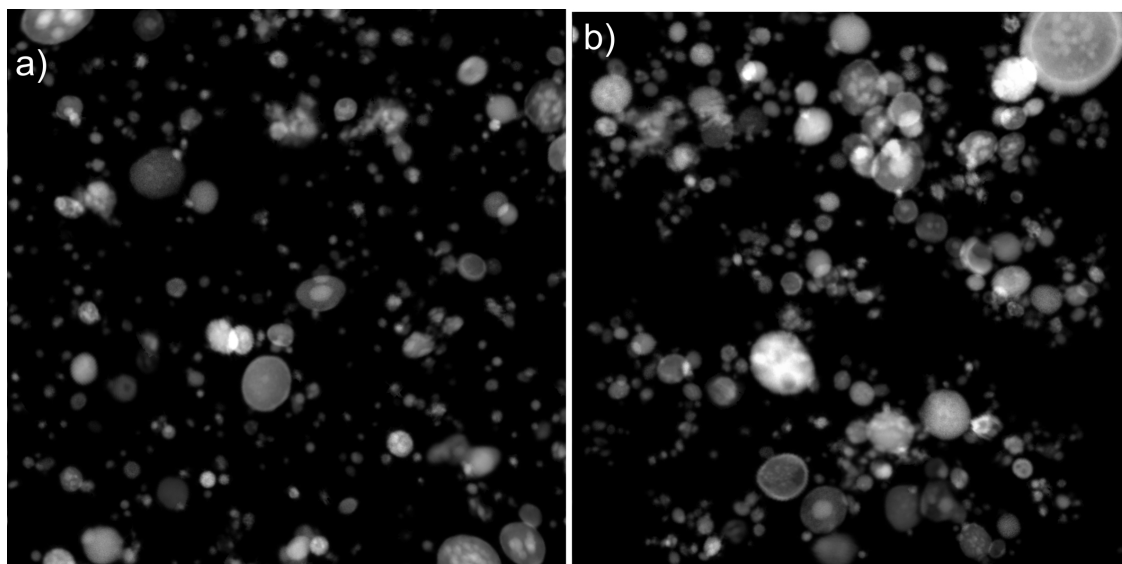


Figure 3: a) Generated image with random placement of extracted Au-Fe, Au-Co NPs, and b) clustered placement, cf. Section 3.3.

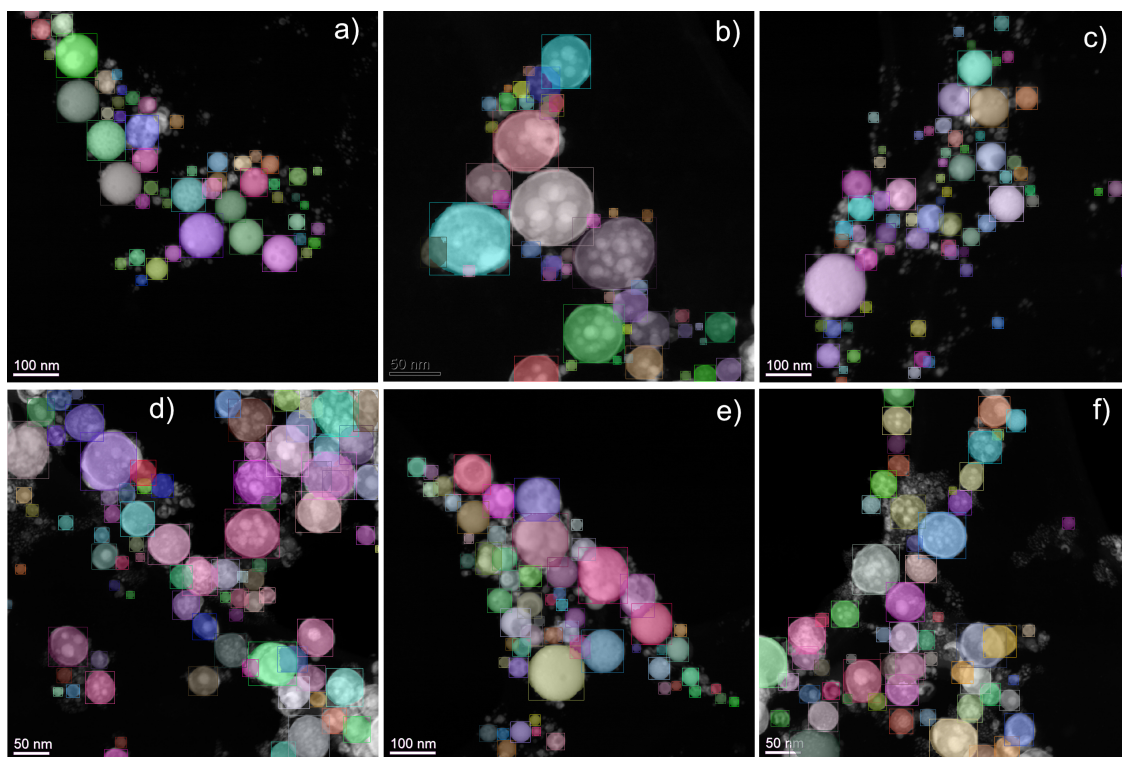


Figure 4: HAADF-STEM images overlaid with detection results filled with different colors for easier viewing from the test in Section 5. Different colors mark individual instances. Best viewed in the digital version, zoom in for more details.

The results are shown in Table 1. We evaluate the impact of the architecture by using different backbone neural networks and their use in the generated images. For each backbone, we compare several versions of the ResNet architecture [22] with 18, 50, and 101 layers. ResNext [24] represents an improvement on the ResNet architecture, which furthermore adds complexity and potential for improvement performance. In our results, we see this improvement between ResNet18 and ResNet50, but no benefit from even more powerful architectures. More complex networks typically require more training data with diminishing returns.

The architecture of the detection part is either plain Mask-RCNN or the improved Cascade Mask-RCNN or Mask Scoring-RCNN or a combination of both extensions. We see that while Mask Scoring-RCNN shows a clear performance benefit of 0.300 MAP against 0.274 MAP, Cascade Mask-RCNN and the combination of both do not show improved performance.

With additional generated annotation in the training set, we see a clear improvement to the 0.33 MAP. The generated images as intended provide useful training data and are realistic enough for the network to transfer the learnings to real images. An interesting additional experiment with only generated images shows roughly the same result with 0.34 MAP. This further confirms the realistic character of the generated images and we must acknowledge that the hand-annotated images are not always as accurate as in the generated images.

Table 1: Detection ablation study. Higher MAP values mean better detection performance.

<b>Architecture</b>	<b>Backend</b>	<b>Data set</b>	<b>MAP</b>
Mask-RCNN	ResNet50	Annotations	0.27
Cascade Mask-RCNN	ResNet50	Annotations	0.25
Mask Scoring-RCNN	ResNet18	Annotations	0.24
Mask Scoring-RCNN	ResNet50	Annotations	0.30
Mask Scoring-RCNN	ResNet101	Annotations	0.26
Mask Scoring-RCNN	ResNeXt101	Annotations	0.24
Cascade Mask Scoring-RCNN	ResNet50	Annotations	0.27
Mask Scoring-RCNN	ResNet50	Annotations + Generated	<b>0.33</b>
Mask Scoring-RCNN	ResNet50	Generated	<b>0.34</b>

#### 4 Ultrastructure classification

For the classification of the NPs ultrastructure, we use a feed-forward deep neural network with three output classes, CS, SoSo as explained in the introduction, and nested core shell (NCS) for NPs which are neither CS or SoSo, but show a contrast variation. HAADF-STEM images of the respective ultrastructures are given in Figure 1a) i-iv). For more details on the structure of NPs and their importance in the development of the formation mechanism, see Kamp et al. [10] as well as Johny et al. [14].

As a compromise between up-scaling smaller NPs and down-scaling larger NPs, we choose an input size of 48x48 pixel, which is quite small compared to other problems in image classification. The EfficientNet[25] architecture is a scalable state-of-the-art neural network architecture, with configuration B0 the smallest to B8 the largest network. We are using it in configuration B2 because of speed and memory trade-offs. Larger networks may be prone to over-fitting and have increasingly diminishing returns.

When training neural networks, especially for image classification, it is crucial to have a large number of images in the training set with a good diversity to reduce overfitting and for better generalization. For this purpose, traditional data augmentation has been widely used in image classification. These data augmentations consist of a variety of image processing operations such as adjusting brightness and contrast, rotation, flipping, shifting, zooming in and out, and cropping the original image.

Although applying random transformations on images achieves improved classification results, these transformations do not add new or extra information to the training set, they only enforce invariance to these transformations for one particular training example. This is a limitation of the standard data augmentation technique, since, for every new image, it only considers one image and not features of the whole data set or class.

Another limitation of the standard data augmentation is that the combination of data transformation functions must be chosen carefully since some transformations may change the semantic meaning of the images. In our data set, this still

Table 2: Fréchet inception distance (FID) scores and NP ultrastructure classification accuracy for image augmentation.

Data / Generator	FID	Accuracy
Original	-	91.23
Classic augmentation	-	89.08
CVAE	147.84	93.02
CGAN	135.62	93.55
InfoGAN	<b>125.82</b>	<b>94.10</b>

occurs occasionally as some transformations can change the image in a way that the NP appears to be from another class, e.g., due to cropping and contrast changes a CS particle may look like a SoSo particle. This motivates our research towards augmentation with different generative neural networks as previously proposed for different modalities and networks in [26] and [27].

A variational autoencoder [28] consists of an encoder that generates a probability distribution of intermediate representations. The decoder learns to generate images from samples of this distribution. The conditional variational autoencoder (CVAE) extends this model to the latent space for each category by including the label as input to both encoder and decoder.

Generative Adversarial Network (GAN) [29] is a proposed generative model that has shown massive success in generating realistic images from different domains. The Generative Adversarial Network is composed of two adversarial networks: generator and discriminator. The generator receives a latent noise vector from a prior distribution as an input and then learns to generate new images that look like images from a particular data set. On the other hand, the discriminator learns to classify images from the real data set as real images and the generated images as fake ones. The idea of the GAN is to train both the generator and discriminator networks simultaneously, like in a competition.

The GAN architecture can be extended into a conditional GAN [30] by adding a class label as an extra input and making the output dependent on it. Therefore, it can generate different images depending on this class variable, in our case different kinds of ultrastructures.

Information Maximizing GAN (InfoGAN)[31] is another extension of the generative adversarial network that aims for more controllable outputs of the generator. The generator should generate similar outputs to similar inputs and the interpolation between two inputs should generate an output visually in-between the outputs of the two corresponding inputs. This is called disentangled representation and is achieved by adding an extra control variable with a prior as input, secondly by maximizing the mutual information between this control variable and the distribution of the generator, see [31] for details. This makes it possible to identify key directions in the input space of the generator that correspond to changes like shape or brightness in generated images and therefore, we can sample the input space evenly and get a well balanced set of all brightness and shape variations.

## 4.1 Evaluation

Before we evaluate the classification and our augmentation approaches, not only by classification accuracy, we want to analyze the generated NPs. For qualitative results see Figure 5, the NPs from the InfoGAN show much higher variability, less noise, and higher image clarity compared to the VAE results. The CGAN images are similar to the InfoGAN images. For quantitative results, we consider the Fréchet inception distance (FID) [32], which measures the distance between mean and covariance matrix of the feature embeddings of real and generated images. A lower FID correlates with better image quality and more similarity to the original images. We see that the InfoGAN results in the best score and best image quality (Table 2 and Figure 5).

## 5 Test

Besides the quantitative and qualitative analysis of individual parts of a data analysis pipeline for NPs, we want to show experimental results using 30 test images. Each image has an individual scale at a fixed position with nm annotation, generated by the microscope software.

For this test, the NPs are automatically detected using the augmentation trained 101-layer Mask Scoring-RCNN model. Then the scale of the image is extracted from its fixed position and measured using image processing, the annotation is read using tesseract optical character recognition [33, 34]. A circle is fitted into the detected contour of the NP and the diameter of this circle with the scaling factor results in the absolute NP size. This diameter is noted in the histogram shown in Figure 6. Note that NPs below the thermodynamic SoSo-stability limit (15 nm) are not included in this analysis [11]. All detected NPs are extracted and classified using a network described in Section 4 and 3, and the results

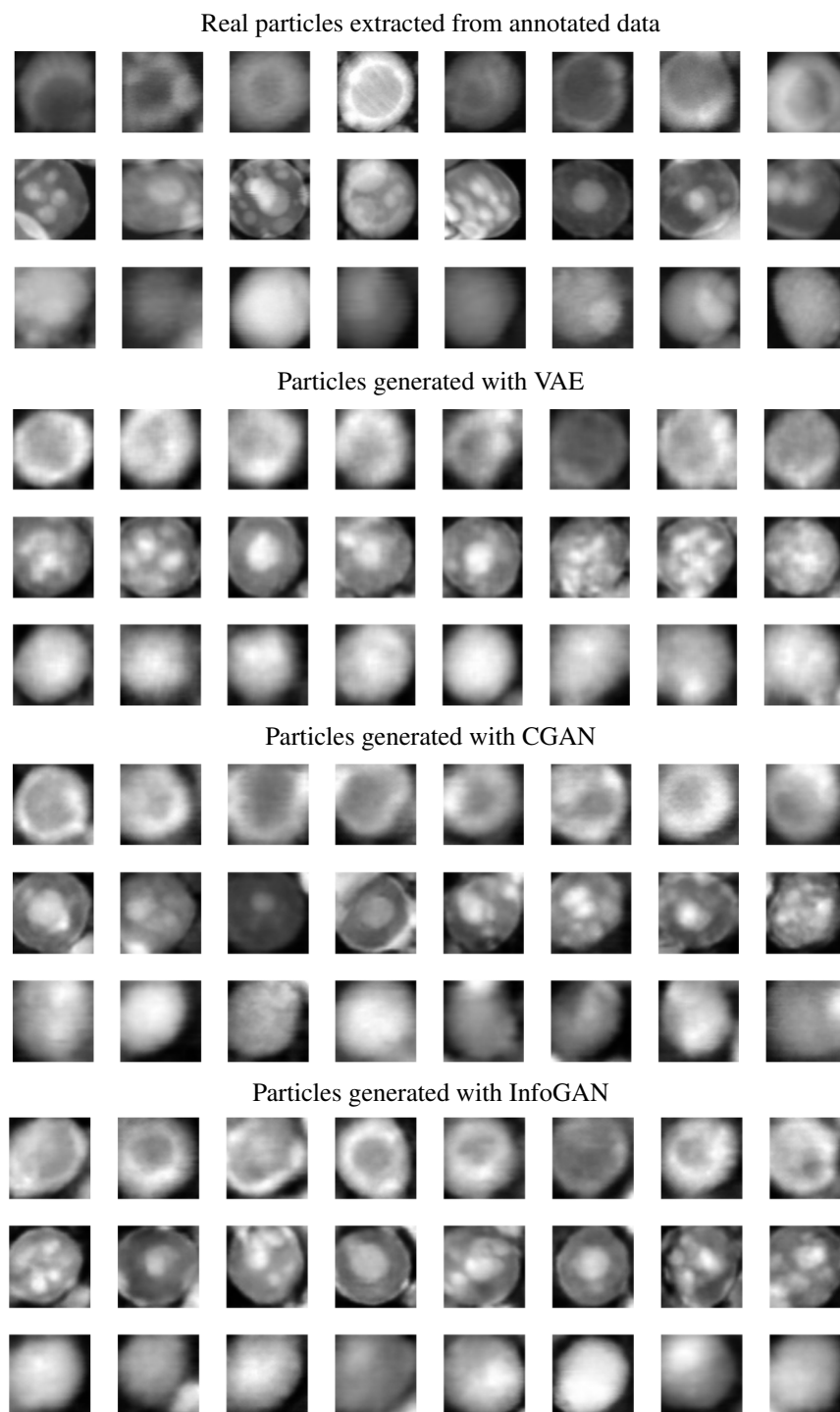


Figure 5: Comparing experimental images of NPs and synthetically generated NPs with CS in the first row, then NCS and SoSo NPs in rows two and three, respectively. The higher clarity, variety, and lower noise in the InfoGAN results compared to VAE are clearly visible. Best viewed in digital format.

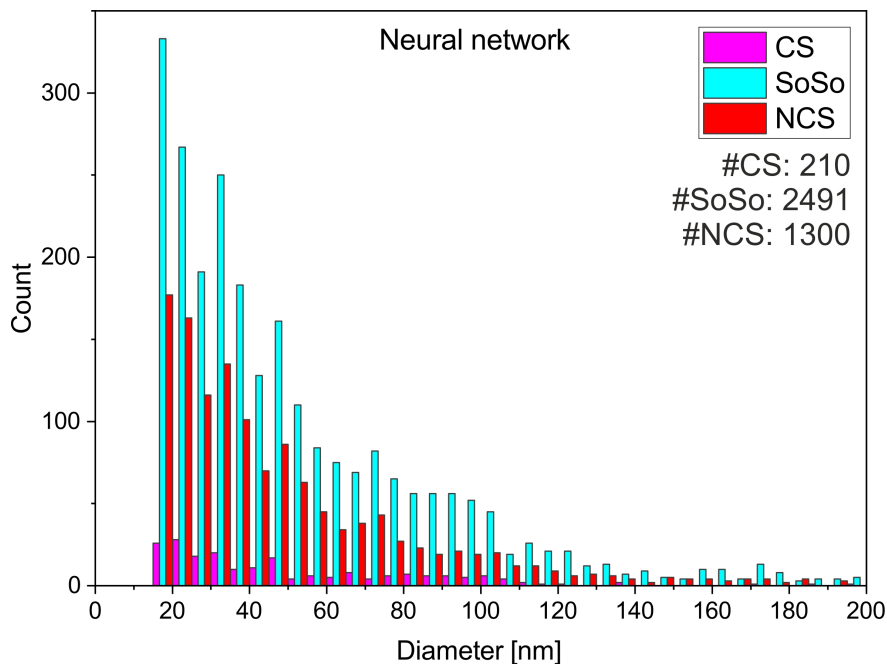


Figure 6: NP size distribution generated by the neural network from 30 test images, with the NP diameter illustrated in a histogram for each particle class. Size distributions include NPs larger 15 nm. The absolute number (#) of NPs is shown in the plot.

are shown in Figure 6. The resulting statistical data is in agreement with the results generated by manual annotation and classification of comparable particle systems. In particular, a Log-normal distribution is generated, which typically represents the size distribution of laser-generated NPs [10, 11, 14]. The size histograms produced by the neural network for different NP ultrastructures are matching their experimentally measured counterparts (cf. 6) and thus show the potential of the developed method in extracting the size and class of individual NPs from complex STEM images.

## 6 Conclusion

In this paper, we present a pipeline for the processing of NPs from STEM imaging. We show, how using a modern architecture, the detection can be handled using deep learning, and how it can be improved using synthetic images. We note a small improvement of 3% in MAP by selecting a more powerful architecture and another 3% using synthetic training data. Another important aspect is classifying the ultrastructure of NPs. We handle this via deep neural networks and show how using GANs to generative synthetic NP images improves the NPs classification performance by 2.9%. Finally, we put all steps together to assemble a pipeline that examines the image from the STEM including automatic scaling, and successfully demonstrate it on 30 images. Such automated generation of size distributions in challenging imaging conditions, including the classification of NPs ultrastructures, will be decisive for research on NPs, especially in highly complex particle systems containing different NP classes in one sample. In particular, multi-parameter synthesis methods such as laser ablation in liquid will benefit greatly from the proposed method, e.g., in the optimization of synthesis parameters and in the subsequent investigation of structure-property relationships.

## 7 Acknowledgements

Dr. A. Piatek is acknowledged for sample preparation. I. Zech and L. Ketelsen are acknowledged for the generation of manual size distributions. In addition, we would like to refer to the project KI 1263/21-1 of the German Research Foundation and would like to acknowledge the funding by the German Research Foundation (project KI 1263/15-1).

## 8 Bibliography

### References

- [1] Caroline A Schneider, Wayne S Rasband, and Kevin W Eliceiri. Nih image to imagej: 25 years of image analysis. *Nature methods*, 9(7):671–675, 2012.
- [2] Wojciech Samek, Thomas Wiegand, and Klaus-Robert Müller. Explainable artificial intelligence: Understanding, visualizing and interpreting deep learning models. *arXiv preprint arXiv:1708.08296*, 2017.
- [3] William W Stead. Clinical implications and challenges of artificial intelligence and deep learning. *Jama*, 320(11):1107–1108, 2018.
- [4] A Yu Kharin. Deep learning for scanning electron microscopy: Synthetic data for the nanoparticles detection. *Ultramicroscopy*, 219:113125, 2020.
- [5] Vincenzo Amendola, Moreno Meneghetti, Osman M Bakr, Pietro Riello, Stefano Polizzi, Dalaver H Anjum, Stefania Fiameni, Paolo Arosio, Tomas Orlando, Cesar de Julian Fernandez, et al. Coexistence of plasmonic and magnetic properties in au 89 fe 11 nanoalloys. *Nanoscale*, 5(12):5611–5619, 2013.
- [6] Dongshi Zhang, Bilal Gökce, and Stephan Barcikowski. Laser synthesis and processing of colloids: fundamentals and applications. *Chemical reviews*, 117(5):3990–4103, 2017.
- [7] Sung-Jin Cho, Susan M Kauzlarich, Justin Olamit, Kai Liu, Fernande Grandjean, Leila Rebbouh, and Gary J Long. Characterization and magnetic properties of core/shell structured Fe/Au nanoparticles. *Journal of Applied Physics*, 95(11):6804–6806, 2004.
- [8] Young-Wook Jun, Jae-Hyun Lee, and Jinwoo Cheon. Chemical design of nanoparticle probes for high-performance magnetic resonance imaging. *Angewandte Chemie International Edition*, 47(28):5122–5135, 2008.
- [9] Irene Vassalini, Laura Borgese, Michele Mariz, Stefano Polizzi, Giuliana Aquilanti, Paolo Ghigna, Andrea Sartorel, Vincenzo Amendola, and Ivano Alessandri. Enhanced electrocatalytic oxygen evolution in Au-Fe nanoalloys. *Angewandte Chemie International Edition*, 56(23):6589–6593, 2017.
- [10] Marius Kamp, Anna Tymoczko, Radian Popescu, Ulrich Schürmann, Ruksan Nadarajah, Bilal Gökce, Christoph Rehbock, Dagmar Gerthsen, Stephan Barcikowski, and Lorenz Kienle. Composition and structure of magnetic high-temperature-phase, stable Fe-Au core-shell nanoparticles with zero-valent bcc Fe core. *Nanoscale Advances*, 2(9):3912–3920, 2020.
- [11] Anna Tymoczko, Marius Kamp, Oleg Prymak, Christoph Rehbock, Jurij Jakobi, Ulrich Schürmann, Lorenz Kienle, and Stephan Barcikowski. How the crystal structure and phase segregation of Au-Fe alloy nanoparticles are ruled by the molar fraction and size. *Nanoscale*, 10(35):16434–16437, 2018.
- [12] Anna Tymoczko, Marius Kamp, Christoph Rehbock, Lorenz Kienle, Elti Cattaruzza, Stephan Barcikowski, and Vincenzo Amendola. One-step synthesis of Fe-Au core-shell magnetic-plasmonic nanoparticles driven by interface energy minimization. *Nanoscale Horizons*, 4(6):1326–1332, 2019.
- [13] Jacob Johny, Oleg Prymak, Marius Kamp, Florent Calvo, Se-Ho Kim, Anna Tymoczko, Ayman El-Zoka, Christoph Rehbock, Ulrich Schürmann, Baptiste Gault, et al. Multidimensional thermally-induced transformation of nest-structured complex au-fe nanoalloys towards equilibrium. *Nano Research*, pages 1–12, 2021.
- [14] Jacob Johny, Marius Kamp, Oleg Prymak, Anna Tymoczko, Ulf Wiedwald, Christoph Rehbock, Ulrich Schürmann, Radian Popescu, Dagmar Gerthsen, Lorenz Kienle, et al. Formation of Co-Au core-shell nanoparticles with thin gold shells and soft magnetic  $\epsilon$ -cobalt cores ruled by thermodynamics and kinetics. *The Journal of Physical Chemistry C*, 125(17):9534–9549, 2021.
- [15] Kai Chen, Jiaqi Wang, Jiangmiao Pang, Yuhang Cao, Yu Xiong, Xiaoxiao Li, Shuyang Sun, Wansen Feng, Ziwei Liu, Jiarui Xu, Zheng Zhang, Dazhi Cheng, Chenchen Zhu, Tianheng Cheng, Qijie Zhao, Buyu Li, Xin Lu, Rui Zhu, Yue Wu, Jifeng Dai, Jingdong Wang, Jianping Shi, Wanli Ouyang, Chen Change Loy, and Dahua Lin. MMDetection: Open mmlab detection toolbox and benchmark. *arXiv preprint arXiv:1906.07155*, 2019.
- [16] Adam Paszke, Sam Gross, Francisco Massa, Adam Lerer, James Bradbury, Gregory Chanan, Trevor Killeen, Zeming Lin, Natalia Gimelshein, Luca Antiga, Alban Desmaison, Andreas Kopf, Edward Yang, Zachary DeVito, Martin Raison, Alykhan Tejani, Sasank Chilamkurthy, Benoit Steiner, Lu Fang, Junjie Bai, and Soumith Chintala. Pytorch: An imperative style, high-performance deep learning library. In H. Wallach, H. Larochelle, A. Beygelzimer, F. d'Alché-Buc, E. Fox, and R. Garnett, editors, *Advances in Neural Information Processing Systems 32*, pages 8024–8035. Curran Associates, Inc., 2019.

- [17] Martín Abadi, Ashish Agarwal, Paul Barham, Eugene Brevdo, Zhifeng Chen, Craig Citro, Greg S. Corrado, Andy Davis, Jeffrey Dean, Matthieu Devin, Sanjay Ghemawat, Ian Goodfellow, Andrew Harp, Geoffrey Irving, Michael Isard, Yangqing Jia, Rafal Jozefowicz, Lukasz Kaiser, Manjunath Kudlur, Josh Levenberg, Dandelion Mané, Rajat Monga, Sherry Moore, Derek Murray, Chris Olah, Mike Schuster, Jonathon Shlens, Benoit Steiner, Ilya Sutskever, Kunal Talwar, Paul Tucker, Vincent Vanhoucke, Vijay Vasudevan, Fernanda Viégas, Oriol Vinyals, Pete Warden, Martin Wattenberg, Martin Wicke, Yuan Yu, and Xiaoqiang Zheng. TensorFlow: Large-scale machine learning on heterogeneous systems, 2015.
- [18] Kaiming He, Georgia Gkioxari, Piotr Dollár, and Ross Girshick. Mask r-cnn. In *Proceedings of the IEEE international conference on computer vision*, pages 2961–2969, 2017.
- [19] Zhaojin Huang, Lichao Huang, Yongchao Gong, Chang Huang, and Xinggang Wang. Mask scoring r-cnn. In *Proceedings of the IEEE/CVF Conference on Computer Vision and Pattern Recognition*, pages 6409–6418, 2019.
- [20] Zhaowei Cai and Nuno Vasconcelos. Cascade r-cnn: high quality object detection and instance segmentation. *IEEE transactions on pattern analysis and machine intelligence*, 2019.
- [21] Olaf Ronneberger, Philipp Fischer, and Thomas Brox. U-net: Convolutional networks for biomedical image segmentation. In Nassir Navab, Joachim Hornegger, William M. Wells, and Alejandro F. Frangi, editors, *Medical Image Computing and Computer-Assisted Intervention – MICCAI 2015*, pages 234–241, Cham, 2015. Springer International Publishing.
- [22] Kaiming He, Xiangyu Zhang, Shaoqing Ren, and Jian Sun. Deep residual learning for image recognition. In *Proceedings of the IEEE conference on computer vision and pattern recognition*, pages 770–778, 2016.
- [23] Tsung-Yi Lin, Michael Maire, Serge Belongie, James Hays, Pietro Perona, Deva Ramanan, Piotr Dollár, and C. Lawrence Zitnick. Microsoft coco: Common objects in context. In David Fleet, Tomas Pajdla, Bernt Schiele, and Tinne Tuytelaars, editors, *Computer Vision – ECCV 2014*, pages 740–755, Cham, 2014. Springer International Publishing.
- [24] Saining Xie, Ross Girshick, Piotr Dollár, Zhuowen Tu, and Kaiming He. Aggregated residual transformations for deep neural networks. In *Proceedings of the IEEE conference on computer vision and pattern recognition*, pages 1492–1500, 2017.
- [25] Mingxing Tan and Quoc Le. Efficientnet: Rethinking model scaling for convolutional neural networks. In *International Conference on Machine Learning*, pages 6105–6114. PMLR, 2019.
- [26] Zhanghao Wu, Shuai Wang, Yanmin Qian, and Kai Yu. Data augmentation using variational autoencoder for embedding based speaker verification. In *INTERSPEECH*, pages 1163–1167, 2019.
- [27] Fabio Henrique Kiyoyiti dos Santos Tanaka and Claus Aranha. Data augmentation using gans. *arXiv preprint arXiv:1904.09135*, 2019.
- [28] Yunchen Pu, Zhe Gan, Ricardo Henao, Xin Yuan, Chunyuan Li, Andrew Stevens, and Lawrence Carin. Variational autoencoder for deep learning of images, labels and captions. *Advances in neural information processing systems*, 29:2352–2360, 2016.
- [29] Ian J. Goodfellow, Jean Pouget-Abadie, Mehdi Mirza, Bing Xu, David Warde-Farley, Sherjil Ozair, Aaron Courville, and Yoshua Bengio. Generative adversarial nets. In *Proceedings of the 27th International Conference on Neural Information Processing Systems - Volume 2, NIPS’14*, page 2672–2680, Cambridge, MA, USA, 2014. MIT Press.
- [30] Mehdi Mirza and Simon Osindero. Conditional generative adversarial nets. *arXiv:1411.1784*, 2014.
- [31] Xi Chen, Yan Duan, Rein Houthoofd, John Schulman, Ilya Sutskever, and Pieter Abbeel. Infogan: interpretable representation learning by information maximizing generative adversarial nets. In *Proceedings of the 30th International Conference on Neural Information Processing Systems*, pages 2180–2188, 2016.
- [32] Martin Heusel, Hubert Ramsauer, Thomas Unterthiner, Bernhard Nessler, and Sepp Hochreiter. Gans trained by a two time-scale update rule converge to a local nash equilibrium. In *Proceedings of the 31st International Conference on Neural Information Processing Systems*, pages 6629–6640, 2017.
- [33] Ray Smith. An overview of the tesseract ocr engine. In *Ninth international conference on document analysis and recognition (ICDAR 2007)*, volume 2, pages 629–633. IEEE, 2007.
- [34] Chirag Patel, Atul Patel, and Dharmendra Patel. Optical character recognition by open source ocr tool tesseract: A case study. *International Journal of Computer Applications*, 55(10):50–56, 2012.